Infrared Spectroscopy at low temperatures and at high magnetic fields

Bo Li(李博)[1], Guidong Guo(郭贵东)[1], Peilin Huang(黄佩霖)[1], Hua Zang(臧华)[1], and Zhi-Guo Chen(谌志国)[1]

[1]Beijing National Laboratory for Condensed Matter Physics and Institute of Physics, Chinese Academy of Sciences, Beijing 100190, China

October 5, 2026

Abstract

Infrared spectroscopy is a powerful experimental tool for investigating the low-energy excitations of matter. Here, we present two setups for infrared spectroscopy measurements in Synergetic Extreme Condition User Facility (SECUF), which includes Setup (I) for infrared measurements at low temperatures (T) and Setup (II) for infrared measurements at high magnetic fields. Therein, Setup (I) can be utilized to perform optical reflectance and transmission measurements down to 5 K in the energy range from 30 to 25000 cm^{-1}, and Setup (II) can be employed to carry out magneto-infrared measurements in Faraday and Voigt geometries at static magnetic fields up to 20 T and at $T = 4.2$ K. Moreover, we showed the examples on the application of these two setups in infrared spectroscopy measurements.

1. Introduction

Infrared spectroscopy is a type of spectroscopic methods detecting the interactions between infrared light and matter via measuring the photon-energy dependent optical constants manifesting the absorption of single-particle excitations or collective excitations [1,2]. Given that low temperature can drive the formation of the ground states of matter, infrared spectroscopy combined with low temperatures can detect optical signatures of ground states, such as superconducting states [3], density wave states [4] and Mott states [5,6]. Considering that high magnetic field can induce Landau levels (LLs) or influence magnetic orders, infrared spectroscopy coupled with high magnetic fields (i.e., magneto-infrared spectroscopy) can measure LL transitions [2] or spin-lattice coupling effects [7]. Thus, infrared spectroscopy combined with low temperatures and magneto-infrared spectroscopy can be used to investigate the exotic physical properties of various quantum materials, e.g., unconventional superconductors [8–10], topological quantum materials [11–19], two-dimensional materials [20] and magnetic van der Waals materials [21].

Here, we introduce two setups for infrared spectroscopy measurements at low temperatures and at high magnetic fields in the Infrared Unit of the THz and Infrared Experimental Station of Synergetic Extreme Condition User Facility (SECUF) (see Fig. 1). Therein, Setup (I) for infrared spectroscopy measurements at



Figure 1: Infrared Unit of the THz and Infrared Experimental Station of Synergetic Extreme Condition User Facility (SECUF).

low temperatures (T), which is mainly composed of a Fourier transform Infrared (FTIR) spectrometer and an optical cryostat, can be employed to obtain optical reflectance and transmission spectra at temperatures down to 5 K in the energy range from 30 to 25000 cm^{-1}. Setup (II) for magneto-infrared spectroscopy measurements, which mainly consists of a FTIR spectrometer, a superconducting magnet and a sample probe, can be used to get optical reflectance and transmission spectra in Faraday and Voigt geometries at static magnetic fields up to 20 T and at $T = 4.2$ K. Additionally, these two setups have been successfully applied in the infrared spectroscopy measurements of two Weyl semimetals $MoTe_2$ and GdPtBi and iron-arsenide superconductor systems NaFeAs and AFe_2As_2 (A = Ba and Ca).

2. Infrared measurement setups

This section is divided into two subsections. We present the setup for low-temperature infrared measurements in subsection 2.1 and the setup for magneto-infrared spectroscopy measurements in subsection 2.2. The key performance parameters and specification of the setups are summarized in Table 1.

Table 1: Key performance parameters and specification of the infrared measurement setups.

Energy Resolution	Spectra Range	Temperature Range	Magnetic Field	Magneto-Infrared Configurations
~ 0.13 cm^{-1}	30—25000 cm^{-1}	4.2—300 K	0—20 T	Faraday, Voigt

2.1. Setup for low-temperature infrared measurements

Since there are algebraic relations among optical quantities, including the complex dielectric function, complex optical conductivity, and complex refractive index (see Table 2), one optical constant can be derived from the other optical constants. Moreover, once the reflectance or transmittance spectrum is measured over a sufficiently broad frequency range, the complex optical response functions—including the complex refractive index, dielectric function, and optical conductivity—can be extracted through Kramers–Kronig analysis combined with the relevant Fresnel relations. Using the setup for low-temperature infrared measurements in the Infrared Unit of the THz and Infrared Experimental Station of SECUF, we can perform the measurements of the reflectance and transmission spectra separately associated with the real parts of the complex reflectivity and complex transmissivity at temperatures down to 5 K in the energy range from 30 to 25000 cm^{-1}.

Table 2: Relations among the optical parameters under vacuum conditions.

Optical parameter	**Complex representation**	**Related expressions**
Dielectric constant	$\hat{\epsilon} = \epsilon_1 + i\epsilon_2$	$\epsilon_1 = \dfrac{n^2 - k^2}{\mu_1}$ $\epsilon_2 = \dfrac{2nk}{\mu_1}$
Conductivity	$\hat{\sigma} = \sigma_1 + i\sigma_2$	$\sigma_1 = \dfrac{nk\omega}{2\pi\mu_1}$ $\sigma_2 = \Big(1 - \dfrac{n^2 - k^2}{\mu_1}\Big)\dfrac{\omega}{4\pi}$
Refractive index	$\hat{N} = n + ik$	$n = \Big\{\dfrac{\mu_1}{2}\big[\epsilon_1^2 + \epsilon_2^2\big]^{\frac{1}{2}} + \dfrac{\epsilon_1\mu_1}{2}\Big\}^{\frac{1}{2}}$ $k = \Big\{\dfrac{\mu_1}{2}\big[\epsilon_1^2 + \epsilon_2^2\big]^{\frac{1}{2}} - \dfrac{\epsilon_1\mu_1}{2}\Big\}^{\frac{1}{2}}$
Reflectivity	$\hat{r} = r_0 e^{i\phi_r}$ $= \dfrac{1 - \hat{N}}{1 + \hat{N}}$ $\phi_r = \arctan\{\dfrac{-2k}{1 - n^2 - k^2}\}$	$R = \lvert\hat{r}\rvert^2 = \dfrac{(1-n)^2 + k^2}{(1+n)^2 + k^2}$
Transmission	$\hat{t} = t_0 e^{i\psi_t}$ $= \dfrac{2}{1 + \hat{N}}$ $\psi_t = \arctan\{\dfrac{-k}{n+1}\}$	$T = \sqrt{\epsilon_1}\,\lvert\hat{t}\rvert^2 = \dfrac{4n}{(n+1)^2 + k^2}$ $= 1 - R$

Figure 2(a) and 2(b) show the setups for low-temperature reflectivity and transmission measurements, respectively. Since gas and water molecules in air induce the strong absorption of infrared light, to minimize the absorption-induced lowering of the intensity of infrared light used for measuring reflectivity and transmission spectra, we utilize a vacuum FTIR spectrometer. Noteworthily, the optical cryostat for low-temperature reflectivity measurements is mounted outside the FTIR spectrometer because the focal length of the concave mirror directly focusing light on the sample is longer than the so-called sample chamber of the FTIR spectrometer (see Fig. 2(c)), while the optical cryostat for low-temperature transmission measurements is insert into the sample chamber of the FTIR spectrometer (see Fig. 2(b)) to make the sample located on the position where the quasi-parallel light from the Michelson interferometer of the FTIR spectrometer is focused (see Fig. 2(d)).

To obtain intrinsic reflectivity and transmission spectra of a sample at temperatures down to 5 K, it is essential to pump the sample chamber of the cryostat to avoid the negative influence of the low-temperature-induced condensation of the water and gasses in the atmosphere on the measurements of reflectivity and transmission spectra, e.g., a dip-like feature arising from the absorption of the ice forming on the sample surface can be present around 3300 cm^{-1} in the reflectivity spectra at temperatures lower than 200 K. Thus, the vacuum degree of the sample chamber of the cryostat usually needs to be better than 3×10^{-5} Pa.

The transmission spectrum of a sample can be obtained by dividing the intensity spectrum of light passing through the sample by the intensity spectrum of light passing through the reference hole with the same size as the sample. Figure 2(d) displays that the sample and the reference hole are separately glued to the tops of the two large holes of a vertical fan-shaped copper sheet with the center of its circle connected by a horizontal stick. The bottom of the horizontal stick is attached by a vertical gear wheel. On the other hand, a horizontal gear

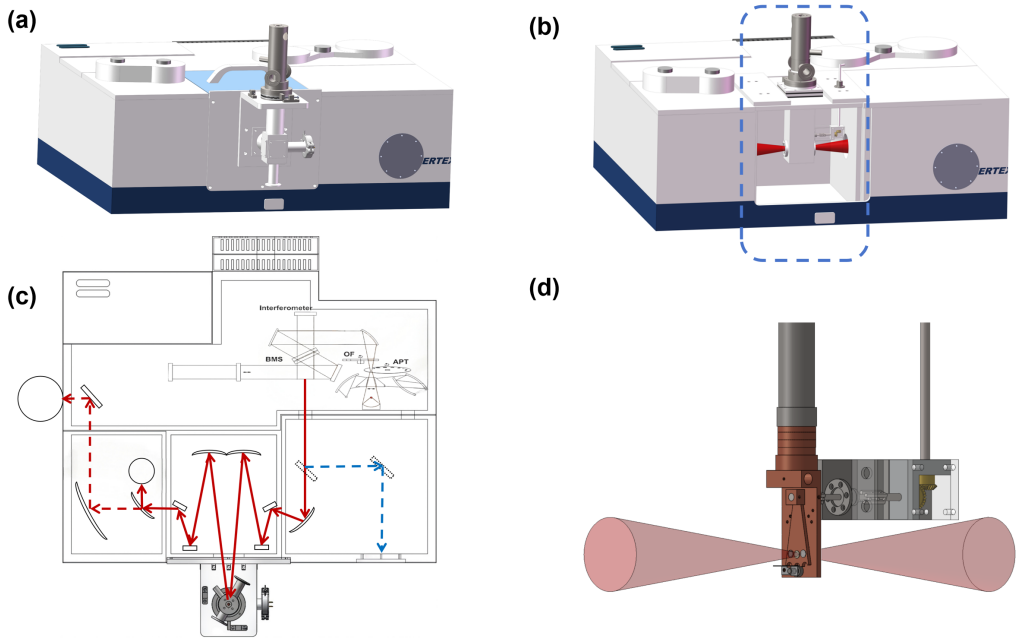


Figure 2: Schematic of the setups for low-temperature infrared measurements. (a) Setup for low-temperature transmission measurements. (b) Setup for low-temperature reflectivity measurements. (c) Optical paths inside the setup for the low-temperature reflectivity measurements. The blue dashed lines denote the optical path for magneto-infrared measurements. (c) Optical path inside the setup for low-temperature reflectivity measurements. The blue dashed lines denote the optical path for magneto-infrared measurements. The red solid lines indicate the optical path for middle-infrared/near-infrared/visible measurements. The red dashed lines represent the optical path for far-infrared measurements. (d) Magnified view of the part indicated by the blue dashed frame in (b), which shows the sample region of the optical cryostat for low-temperature transmission measurements. The positions of the sample and reference can be altered without breaking the vacuum of the FTIR spectrometer.

wheel is attached at the bottom of a vertical stick inserted into the sample chamber of the FTIR spectrometer. The horizontal and vertical gear wheels mesh together, so rotating the vertical stick can switch the sample to the position of the reference hole. More importantly, switching the positions of the sample and reference hole at low temperatures can be realized in a very short time, which can make the measurements of the sample and reference hole in the same setup status and thus can avoid the influence of the drift of the setup status on the transmission measurements at low temperatures.

Furthermore, to eliminate the effect of the unevenness of the sample surfaces on the measurements of reflectivity spectra, we utilized an *in situ* gold and aluminum overcoating technique for measuring reflectivity spectra. The gold or aluminum film coated on the sample surface should not only be thin enough to host the microstructure the same as that of the sample surface but also be thicker than the penetration depth of light into gold or aluminum. Theoretically, the reflectivity spectrum (i.e., R_{sample}) could be obtained via dividing the optical intensity spectrum (i.e., I_{sample}) of the sample by the optical intensity spectrum (i.e., $I_{Au/Al}$) of the gold or aluminum film coated on the sample and then multiplying by the accurate reflectivity spectrum (i.e., $R_{Au/Al}$) of gold or aluminum. However, since there is a time gap between the measurements of the optical intensity

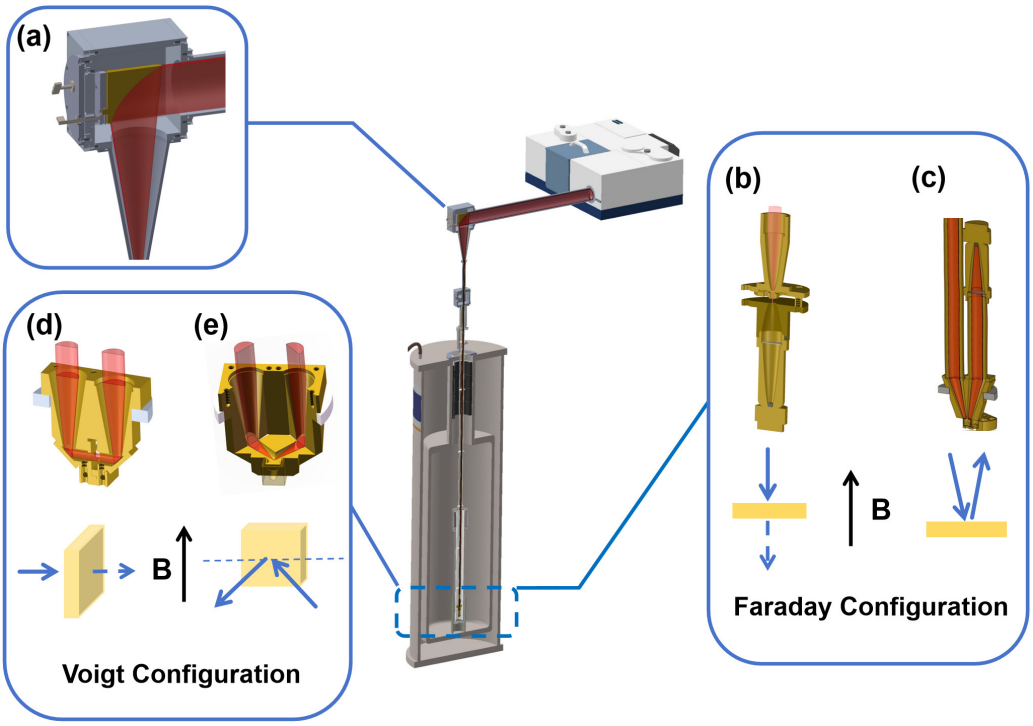


Figure 3: Schematic of the setup for magneto-infrared measurements. (a) Mirror box including a 90° off-axis parabolic gold coated mirror. Gold-coated optical cones for transmission (b) and reflectivity (c) measurements in Faraday configuration. Gold-coated optical cones for transmission (d) and reflectivity (e) measurements in Voigt configuration.

spectra of the sample and the coated gold or aluminum film at the same temperature, a drift of the setup status may take place, which is very likely to influence the accuracy of reflectivity measurements. To compensate the influence of the drift of the setup status on reflectivity measurements, a flat reference mirror made of stainless was employed in the overcoating technique to get the ratios (i.e., I_{sample}/I_{mirror} and $I_{Au/Al}/I_{mirror}$) between the optical intensity spectra of the sample (or coated film) and the reference mirror at the same temperature. Thus, considering the effects of the unevenness of the sample surface and the drift of the setup status on reflectivity measurements, the intrinsic reflectivity spectrum of a sample at low temperature can be given by the relationship: $R_{sample} = [(I_{sample}/I_{mirror})/(I_{Au/Al}/I_{mirror})]\times R_{Au/Al}$.

2.2.Setup for magneto-infrared spectroscopy measurements

The setup for magneto-infrared spectroscopy measurements in the Infrared Unit of the THz and Infrared Experimental Station of SECUF mainly comprises a vacuum FTIR spectrometer, a sample probe and a superconducting magnet. After being reflected by two silver coated concave mirrors, the infrared light from the light source of the FTIR spectrometer becomes quasi-parallel and then is modulated by a Michelson interferometer. The modulated quasi-parallel infrared light passes through the optical pipe and then is cast using a 90° off-axis parabolic gold-coated mirror in a box (see Fig. 3(a)) into an internally polished brass tube of the sample probe. Therein, one side of the optical pipe is connected to the outlet of the vacuum FTIR spectrometer, the other side of the optical pipe is fixed to the mirror box seated directly above the sample probe. Moreover, the optical

pipe, the mirror box and the sample probe are vacuumed to minimize the optical absorption of gas and water molecules. On the top of the sample probe, a wedge diamond window with high transmittance in the infrared range is mounted to maintain the vacuum of the sample probe. Then, the infrared light is focused by the 90° off-axis parabolic gold-coated mirror, passes through the diamond window, and enters an internally polished brass tube of the sample probe. After being reflected by the well-polished inner-surface of the brass tube, the infrared light is condensed by a gold-coated optical cone, which depends on the optical configurations for optical reflectivity and transmission measurements at magnetic fields ($\boldsymbol{B}$). In the optical configuration (i.e., Faraday configuration) for transmission measurements with magnetic field applied in parallel to the wave vector $\boldsymbol{k}$ of incident light (i.e., $\boldsymbol{B}$ // $\boldsymbol{k}$), the infrared light is focused on the surface of the horizontally placed sample by the optical parabolic cone which is vertically mounted and gold coated, transmits through the sample, then becomes divergent and is finally collected by an inner bolometer (i.e., the detector for converting the collected infrared light to electric signals) located at the bottom of the sample probe (see Fig. 3(b)). Different from the Faraday configuration for transmission measurements, the Faraday configuration for reflectance measurements employs a gold-coated optical oblique cone to concentrate the infrared light on the surface of the horizontally placed sample and uses the optical parabolic cone to focus the infrared light reflected by the sample on the chip of the inner bolometer detector mounted above the the optical parabolic cone (see Fig. 3(c)). In the optical configuration (i.e., Voigt configuration) for transmission measurements with magnetic field applied perpendicular to the wave vector of incident light (i.e., $\boldsymbol{B} \perp \boldsymbol{k}$), the infrared light is collected by a vertically mounted and gold-coated optical parabolic cone, is reflected by a planar gold-coated mirror inclined at 45° with respect to the vertical direction, propagates horizontally, transmits through the vertically placed sample, is reflected again by another planar gold-coated mirror, is constrained by another optical parabolic cone and is finally collected by the bolometer detector (see Fig. 3(d)). Discrepant from the Voigt configuration for transmission measurements, the Voigt configuration for reflectance measurements utilizes the planar mirror gold-coated mirror inclined at 45° with respect to the vertical direction and the plane determined by the symmetry axes of the two vertically mounted optical parabolic cones (see Fig. 3(e)).

As an indispensable part of the setup for magneto-infrared spectroscopy measurements, the superconducting magnet mainly includes a superconducting solenoid, a liquid helium chamber and a liquid nitrogen chamber (see Fig. 3). The superconducting solenoid of the magnet, which is fully immersed in the liquid helium inside the liquid helium chamber to enter its superconducting state with high critical electric currents and no loss of electric power, can generate static magnetic fields up to 20 T. The liquid helium in the liquid helium chamber can lower the sample temperature down to 4.2 K when the sample probe with injected helium gas is inserted into the superconducting magnet because the injected helium gas between the probe shell and the measured samples serves as the heat transfer medium. Therefore, the superconducting magnet provides a high-magnetic-field and low-temperature environment for the measured samples. Moreover, the quite low level of the vibrations from the superconducting solenoid and the evaporation of the liquid helium and the liquid nitrogen in the superconducting magnet is beneficial for obtaining the high-quality infrared data with large signal-to-noise ratio.

Using the setup for magneto-infrared spectroscopy measurements, we can measure the intensity spectra of (i) the infrared light reflected by the sample (i.e., $I^R_{sample}(B)$) and (ii) the infrared light passing through the sample (i.e., $I^T_{sample}(B)$) at B from 0 to 20 T. Then, the relative reflectivity (or transmission) spectrum (i.e., $R(B)/R(0$

T) or $T(B)/T(0\ \mathrm{T})$) of the sample can be obtained via dividing the $I^R_{sample}(B)$ (or $I^T_{sample}(B)$) by the $I^R_{sample}(0$ T) (or $I^T_{sample}(0$ T)), i.e., $R(B)/R(0\ \mathrm{T}) = I^R_{sample}(B)/I^R_{sample}(0\ \mathrm{T})$ and $T(B)/T(0\ \mathrm{T}) = I^T_{sample}(B)/I^T_{sample}(0$ T). Thus, multiplying the relative reflectivity (or transmission) spectrum by the zero-magnetic-field reflectivity (or transmission) spectrum gotten via the low-temperature infrared measurements yields the reflectivity (or transmission) spectrum (i.e., $R(B)$ or $T(B)$) in a magnetic field.

3. Applications of the infrared measurement setups

Weyl semimetal, which represent a type of quantum materials hosting pairs of Weyl cones in the bulk and topologically protected Fermi arcs on the surface, have attracted great attention owing to their novel electronic properties and various potential applications [23–31]. Here, using the infrared measurement setups in the Infrared Unit of the THz and Infrared Experimental Station of SECUF, we present the low-temperature infrared spectroscopy measurements of Weyl semimetal $MoTe_2$ and the magneto-infrared spectroscopy measurements of Weyl semimetal GdPtBi.

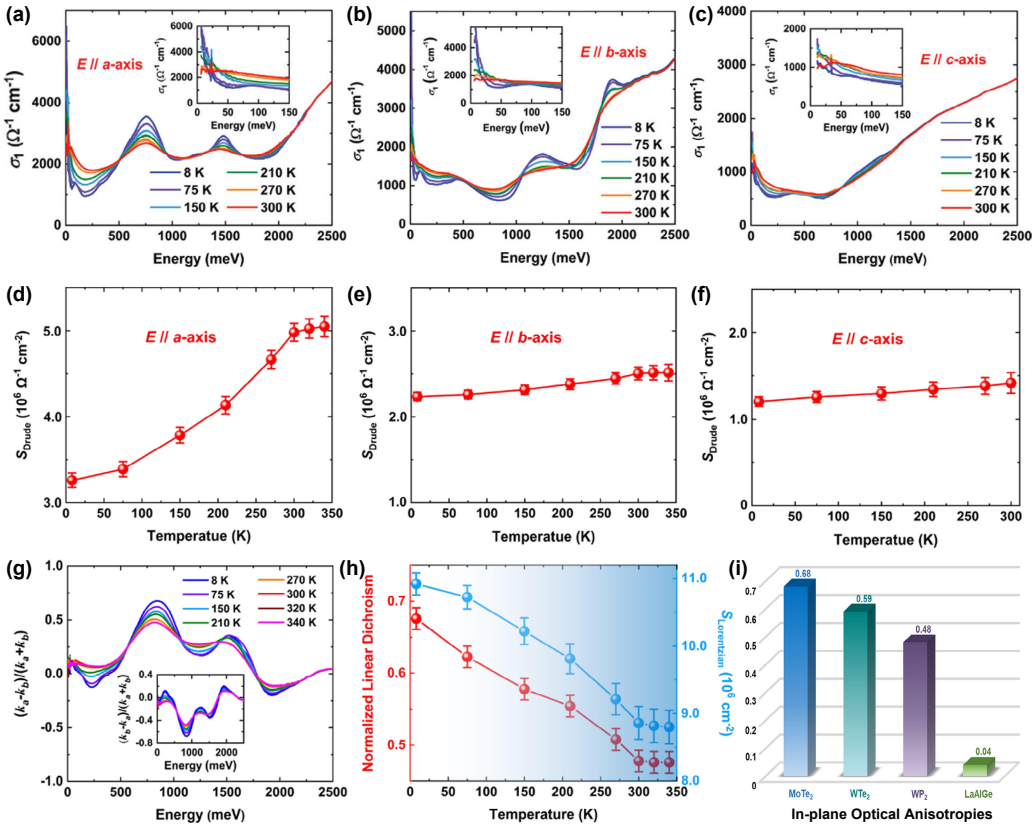


Figure 4: Linearly polarized infrared spectroscopy study of type-II Weyl semimetal $MoTe_2$ at different temperatures [22]. Real parts of the optical conductivity spectra along the *a*-axis (a), *b*-axis (b) and *c*-axis (c). Drude weights along the *a*-axis (d), *b*-axis (e) and *c*-axis (f). (g) Photon energy dependence of the normalized linear dichroism. (h) Normalized linear dichroism at $\sim$ 770 meV (see the red dots) and spectral weight of the Lorentzian peak at $\sim$ 770 meV in the real part of the *a*-axis optical conductivity spectrum. (i) In-plane optical anisotropies (i.e., maximal values of the normalized linear dichroism spectra) of the reported type-II Weyl semimetals $MoTe_2$, WTe_2, WP_2 and LaAlGe.

Weyl semimetal states can be realized by breaking spatial-inversion symmetry or time-reversal symmetry. Structural phase transitions can break spatial inversion symmetry in nonmagnetic semimetals, which can induce a Weyl semimetal state. Investigating the formation mechanism of structural phase transitions inducing Weyl semimetal states will provide important insights into discovering Weyl semimetals. The bulk nonmagnetic semimetal $MoTe_2$ exhibits a monoclinic crystal structure (i.e., the $1T'$ phase belonging to the centrosymmetric space group $P2_1/m$) at temperatures above 250 K. When the temperature drops below 250 K, a structural phase transition accompanied with the breaking of spatial inversion symmetry occurs in semimetal $MoTe_2$ and transforms its monoclinic crystal structure into an orthorhombic structure (i.e., the T_d phase belonging to the noncentrosymmetric space group $Pmn2_1$) exhibiting a type-II Weyl semimetal state [32–36]. Previous theoretical and optical studies indicate that the reduction of the electronic kinetic energy is significant for in the formation of the structural phase transition in semimetal $MoTe_2$ [37–41]. To clarify whether the reduction of electronic kinetic energy after the structural phase transition is anisotropic in this Weyl semimetal, it is essential to study the temperature evolution of the electronic kinetic energy along the in-plane *a*-axis, *b*-axis, and interlayer *c*-axis directions.

Using linearly polarized infrared spectroscopy, Su et al. measured the reflectance spectra of $MoTe_2$ at different temperatures with the electric field ($\boldsymbol{E}$) of the incident light applied separately along the crystalline *a*-axis, *b*-axis and *c*-axis [22]. The real parts of the optical conductivity spectra along the *a*-axis, *b*-axis and *c*-axis were obtained via the Kramers–Kronig transformation of the *a*-axis reflectivity spectrum and the relation between the complex reflectivity and complex optical conductivity (see Fig. 4(a)-(c)). After the structural phase transition, the Drude weight of the *a*-axis optical conductivity spectrum decreases significantly (by ~ 36 % from 300 K to 8 K, corresponding to a lowering of 1.75×10^{-6} Ω^{-1} cm^{-1}, see Fig. 4(d)), whereas the reductions of the Drude weights of the *b*-axis and *c*-axis optical conductivity spectra are much smaller (by about 10 % and 14 %, respectively, from 300 K to 8 K, corresponding to only 2.5×10^{-5} Ω^{-1} cm^{-1} and 2.0×10^{-5} Ω^{-1} cm^{-1}, see Fig. 4(e) and (f)). Since the Drude weight is proportional to electronic kinetic energy, these infrared results indicate that only the electronic kinetic energy along the *a*-axis of $MoTe_2$ decreases significantly after the structural phase transition, while the electronic kinetic energies along the *b*-axis and *c*-axis is weakly reduced, which reveals that one of the driving forces for the occurrence of the structural phase transition leading to the Weyl semimetal state in $MoTe_2$—the reduction of the electronic kinetic energy exhibits strong anisotropy [22].

Due to the the spectral-weight conservation law, after the structural phase transition, the significant reduction in the Drude spectral weight along the *a*-axis and the negligible change of the the Drude spectral weight along the *b*-axis lead to the enhancement of the anisotropy of the interband-transition absorption. Figure 4(g) shows that the renormalized linear dichroism spectra reaches their maxima at ~ 770 meV. Below the structural phase transition temperature, the renormalized linear dichroism value at ~ 770 meV increases with decreasing temperature, which is consistent with the enhancement of the Lorentz peak spectral weight of the *a*-axis optical conductivity spectrum at ~ 770 meV due to the interband transition absorption (see Fig. 4(h)). $MoTe_2$ exhibits by far the largest normalized linear dichroism value (i.e., 0.68 at 8 K) among the reported type-II Weyl semimetals (see Fig. 4(i)) [22,42–44].

A magnetic half-Heusler GdPtBi with its crystal structure belonging to T_d point-group symmetry, hosts four pairs of triple points along its four independent C_3 axes because one doubly degenerate band and two

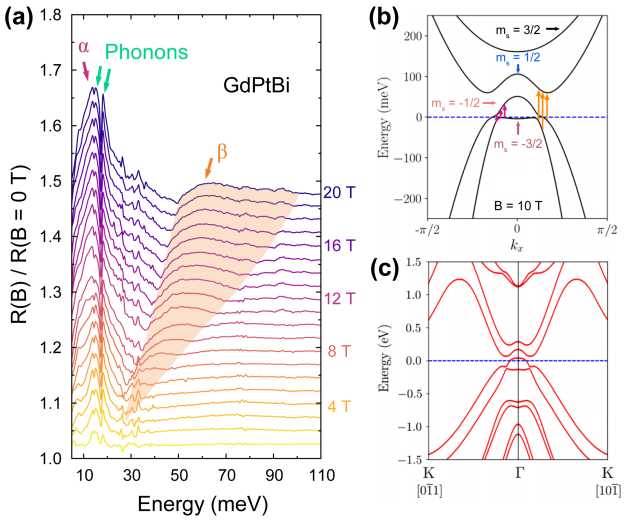


Figure 5: Magneto-infrared spectroscopy study of magnetic-field-induced Weyl semimetal GdPtBi in Faraday configuration (i.e., $\boldsymbol{B}$ // $\boldsymbol{k}$). (a) The relative reflectance spectra $R(B)/R(0\ \mathrm{T})$ of the (111) plane of the GdPtBi single crystal at $T = 4.2\mathrm{K}$ and at magnetic fields up to 20 T. (b) Electronic bands derived from the four-band model reported in Ref. [49]. (c) Band structure obtained by previously reported *ab initio* calculations [49].

nondegenerate bands, which arise from the inversion-symmetry-breaking induced degeneracy-lifting of the Γ_8 bands, cross each other [45]. Upon the application of an external magnetic field to GdPtBi, which breaks time-reversal symmetry, the exchange-interaction-induced Zeeman field causes the splitting of both the Γ_8 and Γ_6 bands and then leads to the emergence of Weyl points [46]. Thus, identify the exchange-interaction-induced splitting of the electronic bands of GdPtBi is a significant step towards the verification of its magnetic-field-induced Weyl semimetal state [47,48].

Using magneto-infrared spectroscopy, we measured the relative reflectance spectra (i.e., $R(B)/R(0\ \mathrm{T})$) of the GdPtBi single crystals at $T = 4.2$ K in Faraday configuration (i.e., $\boldsymbol{B}$ // $\boldsymbol{k}$) at magnetic fields up to 20 T. Figure 5(a) shows that beside the two phonon-like features (labeled by the two green arrows) around $\sim$ 14.6 meV and $\sim$ 18.2 meV, two broad peaks (α and β) indicated by the red and orange arrows are present in the $R(B)/R(0\ \mathrm{T})$ of GdPtBi: (i) a peak-like feature around 15 meV and (ii) a hump-like feature distinctly moving to higher energies with the increase of the magnetic field, which is in agreement with the reported magneto-infrared data measured at magnetic fields up to 16 T [49]. Figure 5(b) displays that the energy distance between the $m_s = \pm 3/2$ bands produced by the four band model in Ref. [49] is distinctly larger than that between the $m_s = \pm 1/2$ bands so that (i) the $m_s = -3/2$ band hybridizes with the $m_s = \pm 1/2$ bands. The hybridization between the $m_s = -3/2$ band and the $m_s = \pm 1/2$ bands results in two energy gaps, which is consistent with the band structure obtained by *ab initio* calculations (see Fig. 5(c)), so (i) the β peak remarkably shifting toward higher energies with the enhancement of the magnetic field can be mainly attributed to the optical transition from the $m_s = -3/2$ (or $m_s = -1/2$) band to the $m_s = 1/2$ band (see the orange arrows in Fig. 5(b)), and (ii) the α peak almost around a fixed energy can be primarily ascribed to the optical transition from the $m_s = -3/2$ band to the $m_s = -1/2$ band (see the red arrow in Fig. 5(b)). Thus, the magneto-infrared results provides spectroscopic evidence for the exchange-interaction-induced splitting of the electronic bands of GdPtBi.

Beyond the studies of Weyl fermions in topological semimetals, magneto-infrared spectroscopy provides

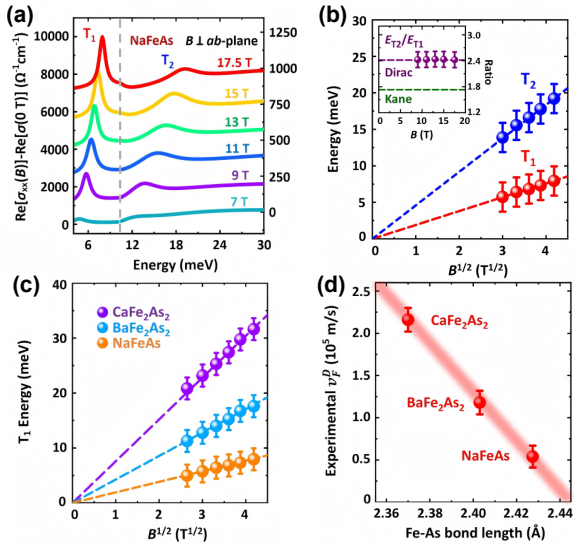


Figure 6: Magneto-infrared spectroscopy study of two-dimensional massless Dirac fermions in iron-arsenide superconductor systems [10]. (a) Relative real part of the optical conductivity of NaFeAs measured in Faraday configuration ($\mathbf{B}\,//\,\mathbf{k}$) at $T = 4.2$ K. (b) T_1 and T_2 energies as functions of $\sqrt{B}$. The inset shows the energy ratio E_{T_2}/E_{T_1} as a function of magnetic field. The purple and green dashed lines denote the theoretical ratios expected for massless Dirac and Kane fermions, respectively. (c) T_1 transition energies of NaFeAs, $BaFe_2As_2$, and $CaFe_2As_2$ as functions of $\sqrt{B}$. (d) Linear scaling relation between the Fermi velocities v_F of two-dimensional massless Dirac fermions and the Fe–As bond lengths.

a powerful probe of massless Dirac fermions in iron-based superconductors. Lv *et al.* measured the relative reflectance spectra of NaFeAs single crystals in Faraday configuration at $T = 4.2$ K and magnetic fields up to 17.5 T [10]. As shown in Fig. 6(a), two peak-like absorption features, labeled as T_1 and T_2, emerge in the relative real part of the optical conductivity. The T_1 and T_2 energies exhibit linear dependences on $\sqrt{B}$ and zero-energy intercepts at $\boldsymbol{B} = 0$ T under linear extrapolations [see Fig. 6(b)]. Moreover, the energy ratio E_{T_2}/E_{T_1} is approximately 2.4, which is close to the energy ratio (i.e., $1 + \sqrt{2}$) between the inter-Landau-level (LL) transitions (i.e., LL_{-1} (or LL_{-2}) $\rightarrow$ LL_{+2} (or LL_{-1}) and LL_0 (or LL_{-1}) $\rightarrow$ LL_{+1} (or LL_0)) of two-dimensional massless Dirac fermions and is distinct from the inter-LL-transition-energy ratio obtained by the Kane model. The T_1 feature, which is associated with the inter-LL transition involving the zeroth LL, is markedly stronger than the other LL-transition absorption features. Furthermore, the DFT+DMFT calculations reveal linearly dispersing bands along the k_x and k_y directions, whereas their band dispersions along the k_z direction are rather weak. These experimental and theoretical results indicate the existence of two-dimensional massless Dirac fermions in the superconducting state of NaFeAs. In addition, the T_1 transition energies of $BaFe_2As_2$ and $CaFe_2As_2$ also exhibit linear dependences on $\sqrt{B}$ [see Fig. 6(c)]. According to the expression on the LL energies of two-dimensional massless Dirac fermions, $E_n = \mathrm{sgn}(n)v_F\sqrt{2e\hbar B|n|}$, where $n = 0, \pm1, \ldots$ and v_F is the Fermi velocity, the Fermi velocities of two-dimensional massless Dirac fermions in NaFeAs, $BaFe_2As_2$ and $CaFe_2As_2$ which can be extracted from the slopes of the linear $\sqrt{B}$ dependences of the T_1 transition energies, are $\sim 0.54 \times 10^5$ m/s, $\sim 1.18 \times 10^5$ m/s and $\sim 2.16 \times 10^5$ m/s. Remarkably, the extracted Fermi velocities exhibit a linear scaling relation with the Fe–As bond lengths [see Fig. 6(d)], which establishes a direct connection

between the lattice degree of freedom and the electronic properties of two-dimensional massless Dirac fermions in iron-based superconductors.

4. Summary

Two setups for infrared spectroscopy measurements in the Infrared Unit of the THz and Infrared Experimental Station of SECUF are introduced in this review article. Therein, the setup for low-temperature infrared measurements mainly consists of the FTIR spectrometer and the optical cryostat and can be used to measure optical reflectance and transmission spectra at temperatures down to 5 K in the energy range from 30 to 25000 cm^{-1}. Furthermore, the setup for low-temperature infrared measurements has been employed to study the temperature evolutions of (i) the electronic kinetic energies along the in-plane *a*-axis, *b*-axis, and interlayer *c*-axis directions of type-II Weyl semimetal $MoTe_2$ and (ii) its relative linear dichroism. The setup for magneto-infrared measurements is mainly composed of the FTIR spectrometer, the superconducting magnet and the sample probe and can be utilized to obtain optical reflectance and transmission spectra in Faraday and Voigt geometries at static magnetic fields up to 20 T and at $T = 4.2$ K. In addition, the setup for magneto-infrared measurements has been applied in studying the exchange-interaction-induced splitting of the electronic bands of magnetic-field-induced Weyl semimetal GdPtBi and two-dimensional massless Dirac fermions in iron-arsenide superconductor systems NaFeAs and AFe_2As_2 (A = Ba and Ca). In the future, we plan to develop polarization-resolved magneto-infrared spectroscopy at this station to perform linear-polarization-resolved and circular-polarization-resolved magneto-infrared measurements, which are expected to gain insight into the interesting physical properties of quantum materials, such as spin-polarization, anisotropy and chirality.

Acknowledgements. The authors acknowledge support from the Guangdong Basic and Applied Basic Research Foundation (Projects No. 2021B1515130007), the National Natural Science Foundation of China (Grant No. 12574180), the National Key Research and Development Program of China (Grant No. 2022YFA1403800), and the Synergetic Extreme Condition User Facility (SECUF, https://cstr.cn/31123.02.SECUF)—Infrared Unit in THz and Infrared Experimental Station.

References

[1] Basov D N, Averitt R D, Van Der Marel D, Dressel M and Haule K 2011 *Rev. Mod. Phys.* **83** 471–541

[2] Akrap A and Orlita M 2026 *Contemp. Phys.* **67** 40–58

[3] Basov D N and Timusk T 2005 *Rev. Mod. Phys.* **77** 721–779

[4] Grüner G 1994 *Density Waves in Solids* (Addison-Wesley, Reading, Mass.)

[5] Kim B J, Jin H, Moon S J, Kim J Y, Park B G, Leem C S, Yu J, Noh T W, Kim C, Oh S J, Park J H, Durairaj V, Cao G and Rotenberg E 2008 *Phys. Rev. Lett.* **101** 076402

[6] Kim S Y, Lee M C, Han G, Kratochvilova M, Yun S, Moon S J, Sohn C, Park J G, Kim C and Noh T W 2018 *Adv. Mater.* **30** 1704777

[7] Tchernyshyov O and Chern G W 2011 Spin-Lattice Coupling in Frustrated Antiferromagnets, in *Introduction to Frustrated Magnetism* (Springer, Berlin, Heidelberg) pp. 269–291

[8] Chen Z G, Dong T, Ruan R H, Hu B F, Cheng B, Hu W Z, Zheng P, Fang Z, Dai X and Wang N L 2010 *Phys. Rev. Lett.* **105** 097003

[9] Chen Z G, Wang L, Song Y, Lu X, Luo H, Zhang C, Dai P, Yin Z, Haule K and Kotliar G 2017 *Phys. Rev. Lett.* **119** 096401

[10] Lv C, Zhao J, Xu Y, Song Y, Zhang C, Ozerov M, Dai P, Wang N L and Chen Z G 2025 *Phys. Rev. B* **111** L241110

[11] Bordács S, Checkelsky J G, Murakawa H, Hwang H Y and Tokura Y 2013 *Phys. Rev. Lett.* **111** 166403

[12] Akrap A, Hakl M, Tchoumakov S, Crassee I, Kuba J, Goerbig M O, Homes C C, Caha O, Novák J, Teppe F, Desrat W, Koohpayeh S, Wu L, Armitage N P, Nateprov A, Arushanov E, Gibson Q D, Cava R J, Van Der Marel D, Piot B A, Faugeras C, Martinez G, Potemski M and Orlita M 2016 *Phys. Rev. Lett.* **117** 136401

[13] Chen Z G, Chen R Y, Zhong R D, Schneeloch J, Zhang C, Huang Y, Qu F, Yu R, Li Q, Gu G D and Wang N L 2017 *PNAS* **114** 816–821

[14] Krizman G, Assaf B A, Phuphachong T, Bauer G, Springholz G, De Vaulchier L A and Guldner Y 2018 *Phys. Rev. B* **98** 245202

[15] Nedoliuk I O, Hu S, Geim A K and Kuzmenko A B 2019 *Nat. Nanotechnol.* **14** 756–761

[16] Xu Y, Zhao J, Yi C, Wang Q, Yin Q, Wang Y, Hu X, Wang L, Liu E, Xu G, Lu L, Soluyanov A A, Lei H, Shi Y, Luo J and Chen Z G 2020 *Nat. Commun.* **11** 3985

[17] Jiang Y, Wang J, Zhao T, Dun Z L, Huang Q, Wu X S, Mourigal M, Zhou H D, Pan W, Ozerov M, Smirnov D and Jiang Z 2020 *Phys. Rev. Lett.* **125** 046403

[18] Shao Y, Rudenko A N, Hu J, Sun Z, Zhu Y, Moon S, Millis A J, Yuan S, Lichtenstein A I, Smirnov D, Mao Z Q, Katsnelson M I and Basov D N 2020 *Nat. Phys.* **16** 636–641

[19] Lv C and Chen Z G 2025 *Rev. Sci. Instrum.* **96** 123905

[20] Rogalski A, Kopytko M and Martyniuk P 2019 *Appl. Phys. Rev.* **6** 021316

[21] Park J G, Zhang K X, Cheong H, Kim J H, Belvin C A, Hsieh D, Ning H and Gedik N 2026 *Rev. Mod. Phys.* **98** 025003

[22] Su B, Wu W, Zhao J, Deng X, Li W, Yang S A, Shi Y, Li Q, Luo J, Gu G and Chen Z G 2025 *Laser Photon. Rev.* **19** 2400599

[23] Wan X, Turner A M, Vishwanath A and Savrasov S Y 2011 *Phys. Rev. B* **83** 205101

[24] Burkov A A and Balents L 2011 *Phys. Rev. Lett.* **107** 127205

[25] Weng H, Fang C, Fang Z, Bernevig B A and Dai X 2015 *Phys. Rev. X* **5** 011029

[26] Yang L X, Liu Z K, Sun Y, Peng H, Yang H F, Zhang T, Zhou B, Zhang Y, Guo Y F, Rahn M, Prabhakaran D, Hussain Z, Mo S-K, Felser C, Yan B and Chen Y L 2015 *Nat. Phys.* **11** 728–732

[27] Soluyanov A A, Gresch D, Wang Z, Wu Q S, Troyer M, Dai X and Bernevig B A 2015 *Nature* **527** 495–498

[28] Lv B Q, Weng H M, Fu B B, Wang X P, Miao H, Ma J, Richard P, Huang X C, Zhao L X, Chen G F, Fang Z, Dai X, Qian T and Ding H 2015 *Phys. Rev. X* **5** 031013

[29] Xu S Y, Belopolski I, Alidoust N, Neupane M, Bian G, Zhang C, Sankar R, Chang G, Yuan Z, Lee C C, Huang S M, Zheng H, Ma J, Sanchez D S, Wang B K, Bansil A, Chou F, Shibayev P P, Lin H, Jia S and Hasan M Z 2015 *Science* **349** 613–617

[30] Shekhar C, Nayak A K, Sun Y, Schmidt M, Nicklas M, Leermakers I, Zeitler U, Skourski Y, Wosnitza J, Liu Z, Chen Y, Schnelle W, Borrmann H, Grin Y, Felser C and Yan B 2015 *Nat. Phys.* **11** 645–649

[31] Zhang C L, Xu S Y, Wang C M, Lin Z, Du Z Z, Guo C, Lee C C, Lu H, Feng Y, Huang S M, Chang G, Hsu C H, Liu H, Lin H, Li L, Zhang C, Zhang J, Xie X C, Neupert T, Hasan M Z, Lu H Z, Wang J and Jia S 2017 *Nat. Phys.* **13** 979–986

[32] Hughes H P and Friend R H 1978 *J. Phys. C: Solid State Phys.* **11** L103–L105

[33] Clarke R, Marseglia E and Hughes H P 1978 *Philos. Mag. B* **38** 121–126

[34] Deng K, Wan G, Deng P, Zhang K, Ding S, Wang E, Yan M, Huang H, Zhang H, Xu Z, Denlinger J, Fedorov A, Yang H, Duan W, Yao H, Wu Y, Fan S, Zhang H, Chen X and Zhou S 2016 *Nat. Phys.* **12** 1105–1110

[35] Huang L, McCormick T M, Ochi M, Zhao Z, Suzuki M-T, Arita R, Wu Y, Mou D, Cao H, Yan J, Trivedi N and Kaminski A 2016 *Nat. Mater.* **15** 1155–1160

[36] Jiang J, Liu Z K, Sun Y, Yang H F, Rajamathi C R, Qi Y P, Yang L X, Chen C, Peng H, Hwang C C, Sun S Z, Mo S K, Vobornik I, Fujii J, Parkin S S P, Felser C, Yan B H and Chen Y L 2017 *Nat. Commun.* **8** 13973

[37] Kimura S, Nakajima Y, Mita Z, Jha R, Higashinaka R, Matsuda T D and Aoki Y 2019 *Phys. Rev. B* **99** 195203

[38] Santos-Cottin D, Martino E, Le Mardelé F, Witteveen C, Von Rohr F O, Homes C C, Rukelj Z and Akrap A 2020 *Phys. Rev. Mater.* **4** 021201

[39] Sun Y, Wu S-C, Ali M N, Felser C and Yan B 2015 *Phys. Rev. B* **92** 161107

[40] Tamai A, Wu Q S, Cucchi I, Bruno F Y, Riccò S, Kim T K, Hoesch M, Barreteau C, Giannini E, Besnard C, Soluyanov A A and Baumberger F 2016 *Phys. Rev. X* **6** 031021

[41] Wang Z, Gresch D, Soluyanov A A, Xie W, Kushwaha S, Dai X, Troyer M, Cava R J and Bernevig B A 2016 *Phys. Rev. Lett.* **117** 056805

[42] Li P, Wen Y, He X, Zhang Q, Xia C, Yu Z-M, Yang S A, Zhu Z, Alshareef H N and Zhang X-X 2017 *Nat. Commun.* **8** 2150

[43] Xu S Y, Alidoust N, Chang G, Lu H, Singh B, Belopolski I, Sanchez D S, Zhang X, Bian G, Zheng H, Husanu M-A, Bian Y, Huang S M, Hsu C H, Chang T-R, Jeng H-T, Bansil A, Neupert T, Strocov V N, Lin H, Jia S and Hasan M Z 2017 *Sci. Adv.* **3** e1603266

[44] Yao M-Y, Xu N, Wu Q S, Autès G, Kumar N, Strocov V N, Plumb N C, Radovic M, Yazyev O V, Felser C, Mesot J and Shi M 2019 *Phys. Rev. Lett.* **122** 176402

[45] Yang H, Yu J, Parkin S S P, Felser C, Liu C-X and Yan B 2017 *Phys. Rev. Lett.* **119** 136401

[46] Cano J, Bradlyn B, Wang Z, Hirschberger M, Ong N P and Bernevig B A 2017 *Phys. Rev. B* **95** 161306

[47] Hirschberger M, Kushwaha S, Wang Z, Gibson Q, Liang S, Belvin C A, Bernevig B A, Cava R J and Ong N P 2016 *Nat. Mater.* **15** 1161–1165

[48] Shekhar C, Kumar N, Grinenko V, Singh S, Sarkar R, Luetkens H, Wu S-C, Zhang Y, Komarek A C, Kampert E, Skourski Y, Wosnitza J, Schnelle W, McCollam A, Zeitler U, Kübler J, Yan B, Klauss H-H, Parkin S S P and Felser C 2018 *PNAS* **115** 9140–9144

[49] Polatkan S, Uykur E, Mohelsky I, Wyzula J, Orlita M, Shekhar C, Felser C, Dressel M and Pronin A V 2023 *Phys. Rev. B* **108** L201201